# Optimizing Interface Conductivity in Electronics

# Constructing CsPbBr₃ Cluster Passivated-Triple Cation Perovskite for Highly Efficient and Operationally Stable Solar Cells

*Wenke Zhou, Shulin Chen, Yicheng Zhao, Qi Li, Yao Zhao, Rui Fu, Dapeng Yu, Peng Gao, and Qing Zhao\**

Ion migration and phase segregation, in mixed-cation/anion perovskite materials, raises a bottleneck for its stability improvement in solar cells operation. Here, the synergetic effect of electric field and illumination on the phase segregation of $Cs_{0.05}FA_{0.80}MA_{0.15}Pb(I_{0.85}Br_{0.15})_3$ (CsFAMA) perovskite is demonstrated. CsFAMA perovskite with a CsPbBr₃-clusters passivated structure is realized, in which CsPbBr₃-clusters are located at the surface/interface of CsFAMA grains. This structure is realized by introducing a CsPbBr₃ colloidal solution into the CsFAMA precursor. It is found that CsPbBr₃ passivation greatly suppresses phase segregation in CsFAMA perovskite. The resultant passivated CsFAMA also exhibits a longer photoluminescence lifetime due to reduced defect state densities, produces highly efficient TiO₂-based planar solar cells with 20.6% power conversion efficiency and 1.195 V open-circuit voltage. The optimized devices do not suffer from a fast burn-in degradation and retain 90% of their initial performance at maximum power under one-sun illumination at 25 °C (65 °C) exceeding 500 h (100 h) of continuous operation. This result represents the most stable output among CsFAMA solar cells in a planar structure with Spiro-OMeTAD.

## 1. Introduction

$CH_3NH_3PbI_3$-based hybrid perovskite materials have been developed for efficient photovoltaic devices[1–8] due to their remarkable properties, such as long carrier diffusion length,[9] low exciton binding energy,[10,11] photon recycling,[12] high defect tolerance,[13] and low cost fabrication methods like other photovoltaic materials,[14,15] etc. Replacing $CH_3NH_3^+(MA^+)$ with

formamidinium ($FA^+$) was found to obtain perovskite with better thermal stability,[16] however, $FAPbI_3$ transforms into non-perovskite phase at room temperature.[17] The $FAPbI_3$ phase instability was addressed in cation/anion mixed-perovskite materials $(Cs_xFA_yMA_{1-x-y})Pb(I_zBr_{1-z})$. For the cation/anion mixed perovskite solar cells (PSCs), $[FA]^+$ and $[PbI_3]^-$ constitute the matrix; $MA^+$, cesium ($Cs^+$), and bromide ($Br^-$) are incorporated for excellent structure stability and robust reproducibility.[18–22] However, the long-term instability issue still poses a huge challenge for their commercialization.[23–27] So far, rapid progress has been achieved on the ambient and thermal stability improvement. For example, composition engineering, like $K^+$, $Cd^{2+}$, and $Cl^-$ incorporation,[28,29] can release the lattice strain and increase the formation energy of vacancies; or using long chain molecules/2D perovskite as water resistant layer.[30–33] In addition, contact engineering, such as employment of moisture-blocking layer[34] or inorganic hole transport layer,[35] also contributes to suppressed device degradation against water and thermal heat.

Although the state-of-art CsFAMA PSCs itself can pass accelerated stability test, however, an initial exponential loss followed by a linear decay can be observed under operational condition, even in inertia ($N_2$ or Ar) atmosphere.[27] Excluding the influence of water and oxygen, the degradation probably originates

Dr. W. K. Zhou, Dr. Y. C. Zhao, Dr. Q. Li, Dr. Y. Zhao, Dr. R. Fu,
Prof. D. P. Yu, Prof. Q. Zhao
State Key Laboratory for Mesoscopic Physics
School of Physics
Peking University
Beijing 100871, China
E-mail: zhaoqing@pku.edu.cn
Dr. S. L. Chen, Prof. D. P. Yu, Prof. P. Gao
Electron Microscopy Laboratory
School of Physics
Peking University
Beijing 100871, China

The ORCID identification number(s) for the author(s) of this article can be found under https://doi.org/10.1002/adfm.201809180.

Prof. D. P. Yu, Prof. P. Gao, Prof. Q. Zhao
Collaborative Innovation Center of Quantum Matter
Beijing 100084, China
Prof. D. P. Yu
Institute for Quantum Science and Technology and Department of Physics
South University of Science and Technology of China (SUSTech)
Shenzhen 518055, China
Prof. P. Gao
International Center for Quantum Materials
School of Physics
Peking University
Beijing 100871, China

**ADVANCED
SCIENCE NEWS**

www.advancedsciencenews.com

**ADVANCED
FUNCTIONAL
MATERIALS**

www.afm-journal.de

from ionic motion in perovskite film,[36] under the driven of light and electric field.[26,37] Thus, under operation, the mobile and gradually accumulated ions could cause destruction in device, like phase segregation,[38] interface mismatching[39] or damage of organic hole transport layers.[40] In polycrystalline films, grain boundary (GB) is a major pathway for the motion of ions.[41,42] Therefore, inhibiting ion migration, including GB passivation, is a key route toward highly efficient and operationally stable cation/anion mixed PSCs.

Recently, inorganic cesium lead halide perovskites ($CsPbX_3$), without any organic cation, were found to be much more thermally stable compared to FA/MA counterpart, with boosted efficiency.[43,44] Even better, inorganic PSCs exhibit excellent operational stability with negligible efficiency loss after hundreds of hours' operation under illumination[43] due to light-independent ionic transport property in cesium perovskite.[45] Whereas, large loss-in-potential[46] restrict its development in PSCs. Otherwise, although tiny amount (≈5%) incorporation of inorganic cation into FA/MA matrix can improve device stability,[21] too much $Cs^+$ will come alongside the undesirable increase in bandgap, sacrificing device current. Therefore, developing more stable perovskite layers without comprising PCE is urgently needed.

In this study, phase segregation and ion migration is first identified in CsFAMA system by a combination of in situ photoluminescence (PL) scan and Galvanostatic measurement. Then, we put forward a new structure design to construct a $CsPbBr_3$-clusters passivated perovskite film to combine the high efficiency of CsFAMA and the high stability of inorganic $CsPbBr_3$. In this structure, $CsPbBr_3$ forms as cluster, suppresses ion migration and passivates CsFAMA grains, evidenced by scanning transmission electron microscopy (STEM) energy dispersive X-ray spectroscopy (EDS) mappings, ion migration quantification, and impendence spectra. CsFAMA films with 3% mol of $CsPbBr_3$ additive demonstrate enhanced PL lifetime, decreased defect state density, larger activation energy of ion migration, and suppressed phase segregation. As a result, the passivated PSCs exhibit around 20% stabilized power conversion efficiency without 'burn-in' exponential decay, with a champion open circuit voltage ($V_{oc}$) of 1.195 V. Notably, 1.195 V is the highest $V_{oc}$ for PSCs with bandgap of 1.63 eV in planar-$TiO_2$ structure. Furthermore, the target device achieves significantly extended long-term operational stability by remaining 90% of the initial efficiency after 500 h continuous operation under maximum power point (MPP) and light illumination. More importantly, under both continuous full-sun illumination, MPP operation and thermal stress (65 °C), the passivated PSCs demonstrate a 125 h device lifetime ($T_{80}$), which is the longest thermal operational stability in $TiO_2$-based planar type CsMAFA PSCs.

## 2. Results and Discussion

### 2.1. Synergetic Effect of Electric Field and Light on Phase Segregation in CsFAMA Perovskite Film

Light-induced phase segregation has been widely reported in $MAPb(I_xBr_{1-x})_3$,[38,47] and the lower bandgap phase can act as trap states, which will severely hinder device performance and

stability.[26] For the CsFAMA, however, the phase segregation behavior remains unclear. Considering a strong correlation between ionic motion and phase segregation, and in order to study them in CsFAMA system, in situ PL characterization combined with Galvanostatic measurement were employed (**Figure 1**a). The testing sample is an Au/CsFAMA/Au lateral structure. Both electric field and illumination are applied to imitate the working condition of PSCs. Galvanostatic measurement (Figure 1b) is a standard method to investigate ion migration in ionic conductors.[48] Upon switching the current value of 80 nA, the voltage spontaneously reaches a small value of 1.6 V (region I in Figure 1b), then slowly elevates (region II). Due to progressively accumulated ions near two electrodes, the voltage increases then reaches a saturation value where only electronic conductivity exists (region III). The saturation voltage is 18 V and the gap of two electrodes is 30 μm, which gives an electric field around 0.6 V μm$^{-1}$ across the perovskite film. Previously, it was found that ion migration could be activated at a relative small electric field <1 V μm$^{-1}$.[49] Result shown in Figure 1b strongly indicates that ion migration occurs in CsFAMA film.

Then we characterize phase segregation behavior by in situ PL measurement under electric poling. Before electric poling, the CsFAMA film has a similar PL peak position (≈765 nm) and intensity value in the selected region from anode to cathode (Figure 1c). After current value switches on, the PL intensities on both anode and cathode decrease by nearly one order of magnitude after 100 s poling process. Moreover, the PL peak position shows a visible red shift about 30 nm near the anode side, from 763 to 793 nm (Figure 1d). An obvious blueshift about 50 nm from 765 to 710 nm is observed near the cathode side (Figure 1e). The PL intensity decay accompanied with peak position shift strongly indicates gradually increased defect states and phase segregation under the applied electric field. Ionic transport-induced element redistribution was speculated to be the origin of observed phase segregation. Then, we move on to explore the variation of PL peak position in the entire perovskite film (Figure S1a, Supporting Information). During polling duration, the gradually increased peak position shift behavior (Figure S1b, Supporting Information) indicates an iodide-rich and a bromide-rich phase forming, which gives a strong evidence of halide redistribution in the CsFAMA perovskite film. EDS mappings under scanning electron microscopy (SEM) model (Figure S1c, d, Supporting Information) show different iodide and bromide distribution variation after 80 s polling, in comparison with their initial state. This result is highly consistent with the PL peak shift data shown in Figure S1b in the Supporting Information, and agrees well with our speculation. It is worth to mention that when only electric poling or illumination is present, we do not find obvious phase segregation in CsFAMA, which imply a synergetic effect of electric field and light on it.

### 2.2. Constructing CsPbBr₃-passivated CsFAMA Perovskite Film

Therefore, ion migration induced excess defects and phase segregation could hinder the operational stability of CsFAMA solar cells.[49] Meanwhile, the inorganic cesium lead halide was reported with excellent thermal and light stability.[43,45]
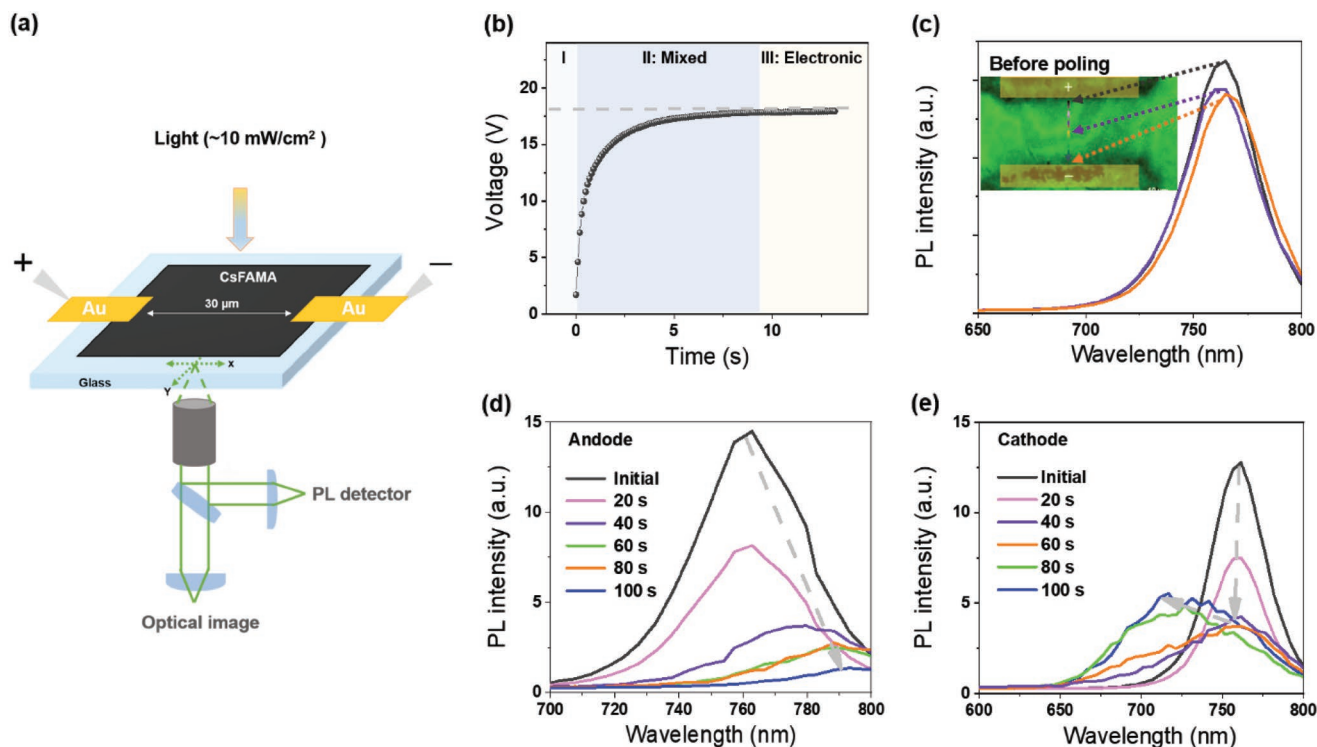
**Figure 1.** Phase segregation characterization of $Cs_{0.05}FA_{0.80}MA_{0.15}Pb(I_{0.85}Br_{0.15})_3$ (CsFAMA) film. a) Schematic illustration of in situ PL characterization with Galvanostatic measurement under light illumination. b) Voltage–time (V–t) curve at Galvanostatic model for a fixed direct current about 80 nA of the lateral structure. Region II depicts the gradually depletion of the mobile ions, and region III depicts the pure electronic conductance in the perovskite. c) PL spectra of the sample before electric poling at three selected positions, as indicated in the inset of the PL emission image. d) PL spectra at the positive pole (anode) after different electric poling durations. e) PL spectra at the negative pole (cathode) after different electric poling durations.

Especially, $CsPbBr_3$ exhibits almost no degradation under illumination, heat, and extreme humidity environment.[50] Here, we develop a novel solution method to design a $CsPbBr_3$-clusters passivated structure, to use the inorganic $CsPbBr_3$ clusters to protect the triple-cation perovskite, combining the good stability of inorganic perovskite and high efficiency of triple-cation perovskite. The schematic of $CsPbBr_3$-passivated precursor method and the structure of perovskite film is depicted in **Figure 2**a. $CsPbBr_3$ precursor solution with different molar ratios were added to the as-prepared CsFAMA precursor solution.[51] Then, the mixed precursor solution was spin coated on the $TiO_2$ substrates by antisolvent method then with an annealing process to form perovskite grains. To simplify the description, hereafter, we refer to the perovskite samples fabricated by usual CsFAMA precursor solution and $CsPbBr_3$-passivated precursor solution as w/o $CsPbBr_3$ and with $CsPbBr_3$, respectively.

To confirm the additive $CsPbBr_3$ precursor solution could induce $CsPbBr_3$-clusters around the formed perovskite grains, detailed STEM EDS mappings was conducted. The high-angle annular dark field (HAADF) and EDS images $CsPbBr_3$ are shown in Figure 2b,c. Here, we choose bromide to indicate the $CsPbBr_3$ distribution and iodide for CsFAMA on energy dispersive spectra. To have an obvious distinguish between different elements, the mapping results of bromide is shown simultaneously with iodide and lead, respectively. For the sample with $CsPbBr_3$, typical bromide distributions were observed as clusters (Figure 2d–g). As highlighted with dashed lines in the two selected regions, large amount of bromide was detected to concentrate like clusters, which strongly indicates a high bromide content accumulated around the bulk perovskite crystals. The excess bromide is due to the contribution from $CsPbBr_3$ additive, in an obvious contrast to the uniform element distribution in the sample of w/o $CsPbBr_3$ (Figure S2, Supporting Information). The results strongly suggest that $CsPbBr_3$ precursor additive form clusters and most of these clusters accumulate at the surface or interface of the bulk CsFAMA grains. As schematized in Figure 2h, the randomly imbedded $CsPbBr_3$ act as clusters around CsFAMA grains, which may protect the core bulk crystal.

Further, in order to figure out whether the added $CsPbBr_3$ could incorporate into crystal structure of CsFAMA or not, normalized X-ray diffraction (XRD) patterns of the perovskite films with different amounts of $CsPbBr_3$ solution additive are shown in Figure S3 (Supporting Information). The XRD spectra peak positions [from (110) to (300)] exhibit an obvious non-linear trend versus $CsPbBr_3$ amount. Meanwhile, XRD spectra of films with $CsPbBr_3$ powder additive as a control experiment, shown in Figure S4 (Supporting Information), gives a linear dependence between the angles of peak position and $CsPbBr_3$ solution content, which could be considered to cause an incorporation of added $Cs^+$ and $Br^-$ into CsFAMA crystal lattice. In contrast with the linear relationship in Figure S4 in the Supporting Information, the non-linear

**ADVANCED
SCIENCE NEWS**
www.advancedsciencenews.com

**ADVANCED
FUNCTIONAL
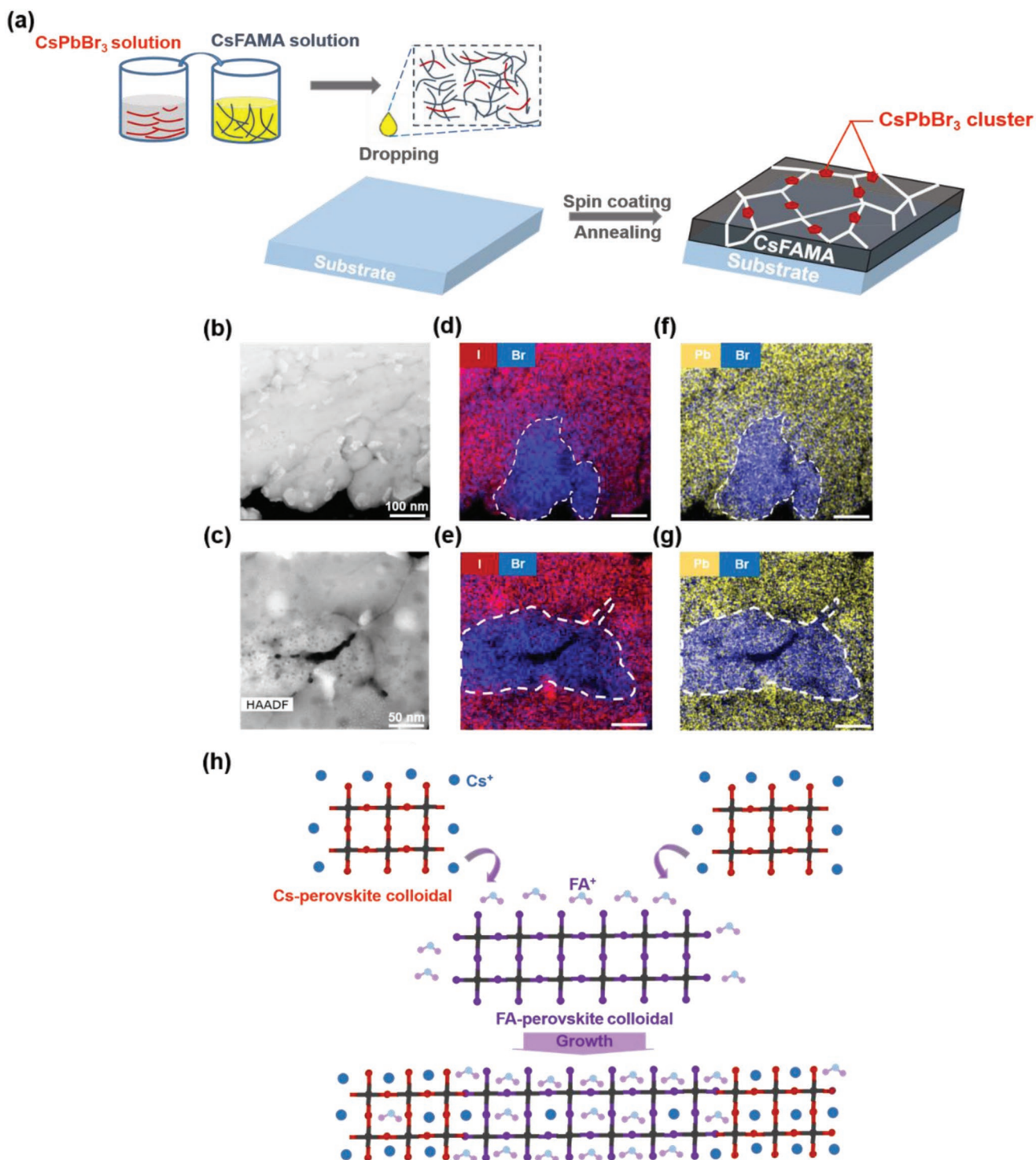MATERIALS**
www.afm-journal.de

**Figure 2.** Scheme and structure characterization of $CsPbBr_3$-cluster passivated perovskite film. a) Scheme of device fabrication process, which involves precursor solution preparation, subsequent spin coating and the final annealing step to form perovskite film. b,c) HAADF image of the perovskite film with $CsPbBr_3$ (3% mol). Scale bar: 100 and 50 nm. d,e) Corresponding EDS mapping of I and Br of the perovskite film. Pink and blue stands for iodide and bromide elements distribution, respectively. f,g) Corresponding EDS mapping of Pb and Br of the perovskite film. Yellow and blue stands for lead and bromide elements distribution, respectively. h) Schematics of perovskite growth through $CsPbBr_3$ colloidal solution additive.

curve in Figure S3 in the Supporting Information strongly suggests that when the amount of $CsPbBr_3$ solution additive is less than 6%, most of the cesium and bromide are located at the surface/interface of CsFAMA grains, and detailed explanations could be found in Supporting Information following Figure S4.

### 2.3. Characterizations of CsPbBr$_3$-Passivated CsFAMA Perovskite Film

To investigate the properties of the CsPbBr$_3$-passivated perovskite films, we carried out morphological, structural, and optical characterizations, respectively. The amount of CsPbBr$_3$ is optimized first and the corresponding results are shown in Figures S5 and S6 (Supporting Information). Top-view SEM images of samples w/o CsPbBr$_3$ and with different ratio of CsPbBr$_3$ show similar morphology, such as coverage, roughness, and grain size. The steady-state PL results of the films show no obvious changes in PL peak position until the amount of CsPbBr$_3$ reached 3 mol% (Figure S6a, Supporting Information). Additionally, we found a maximum efficiency improvement in PSCs with 3% CsPbBr$_3$ additive (Figure S6b, Supporting Information). Therefore, we choose 3 mol% ratio of CsPbBr$_3$ as the target additive value.

Cross-section SEM images of PSCs (**Figure 3**a,b) show a perovskite thickness around 500 nm, which guarantees good light absorption. Moreover, the perovskite grains of device with CsPbBr$_3$ are more vertically monolithic. These uniform grains, going from top to bottom, would lead to fewer charge carrier loss and better charge transport. XRD results of the samples w/o CsPbBr$_3$ and with CsPbBr$_3$ are shown in Figure 3c. Besides, the bandgap of the perovskite maintains its original value with around 1.62 eV, demonstrated by absorbance spectra (Figure 3d). XRD and absorbance results suggest that the sample with CsPbBr$_3$ maintain the basic crystal orientation and chemical composition of the CsFAMA perovskite. Time-resolved PL decay profiles are investigated as well and the PL lifetime is fitted by bi-exponential decay models (Figure 3e), in which a relatively fast decay component (around several nanoseconds) is assigned to charge carrier trapping induced by trap states, while a slower component (around hundreds of nanoseconds) is assigned to free carrier radiative recombination. In contrast to samples w/o CsPbBr$_3$, the samples with CsPbBr$_3$ shows an elongated carrier lifetime from $\tau_1 \approx 6 \pm 2$ ns/$\tau_2 \approx 718 \pm 19$ ns to $\tau_1 \approx 15 \pm 2$ ns/$\tau_2 \approx 934 \pm 21$ ns, implying reduced defect states of passivated perovskite films.

### 2.4. Photovoltaic Performance and Operational/Thermal Stability of CsPbBr$_3$-Passivated CsFAMA Perovskite Solar Cells

Given that the perovskite films with CsPbBr$_3$ has better vertical morphology and longer carrier lifetime in contrast to films w/o CsPbBr$_3$, planar-TiO$_2$-based PSCs were fabricated. **Figure 4**a shows the current density–voltage curves of the champion devices w/o and with CsPbBr$_3$. The fabricated PSCs w/o and with CsPbBr$_3$ exhibit similar short current densities $J_{sc} \approx 22$ mA cm$^{-2}$ and fill factor FF $\approx 76\%$. More importantly, the open-circuit voltage ($V_{oc}$) of the device with CsPbBr$_3$ is around 1.195 V, demonstrating a significant improvement of $\approx$35 meV and a higher power conversion efficiency of 20.6%, compared to $V_{oc} \approx 1.16$ V and PCE $\approx 20.1\%$ of the device w/o CsPbBr$_3$. The PCE and $V_{oc}$ of PSCs with different ratio amount of CsPbBr$_3$ are listed in Figure 4b. As far as is known, 1.195 V is the highest $V_{oc}$ achieved for PSCs with energy bandgap of 1.63 eV in planar-TiO$_2$ structure, corresponding to a loss-in-potential of 0.42 eV. The greatly improved $V_{oc}$ in PSCs strongly indicates reduced defect densities or non-recombination centers, in good agreement with the enhanced PL-lifetime result in passivated perovskite films. $J_{sc}$ value in Figure 4a agrees well with the integrated external
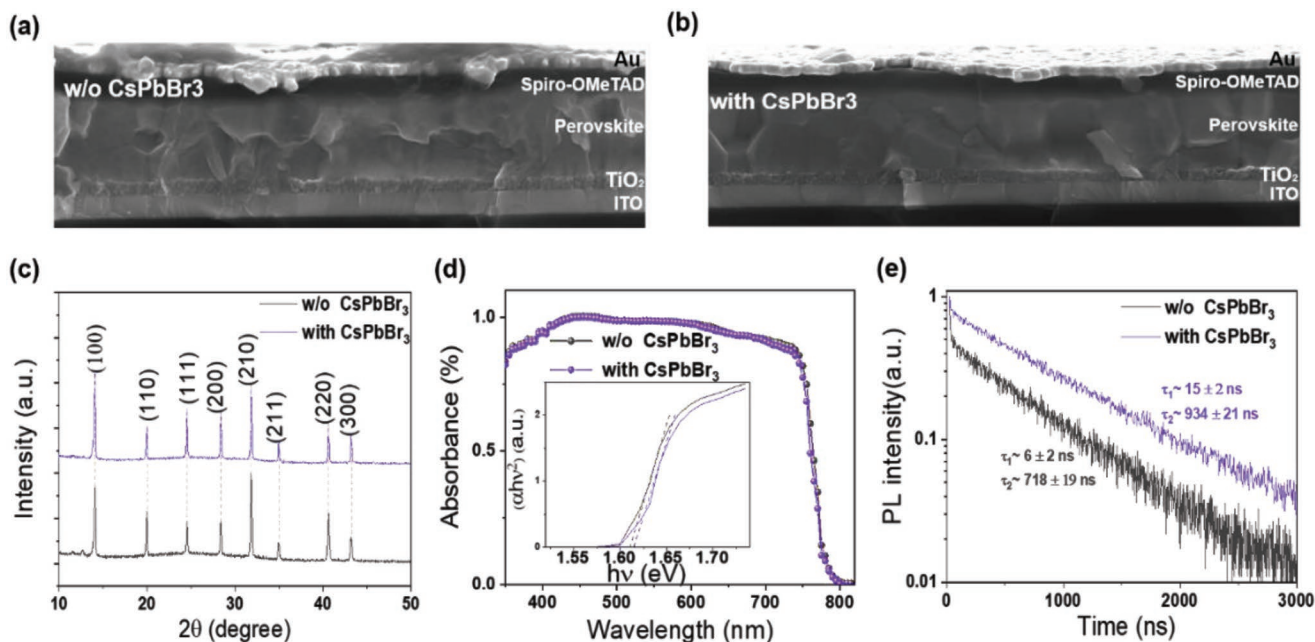


**Figure 3.** Morphological, structural and optical characterization of CsPbBr$_3$-cluster passivated perovskite film. a,b) Cross-sectional SEM images of devices a) w/o CsPbBr$_3$ and b) with CsPbBr$_3$ (3% mol), with the structure of ITO/TiO$_2$/perovskite/Spiro-OMeTAD/Au. c) XRD spectra for the samples w/o CsPbBr$_3$ (dark grey) and with CsPbBr$_3$ (violet). d) Absorption spectra and of the perovskite films w/o CsPbBr$_3$ (dark grey) and with CsPbBr$_3$ (violet). Inset: Tauc plot results of the samples. Dash lines show the fitting curve of linear part of the Tauc plot (Note S1, Supporting Information). e) Time-resolved PL spectra for the perovskite films w/o CsPbBr$_3$ (dark grey) and with CsPbBr$_3$ (violet).
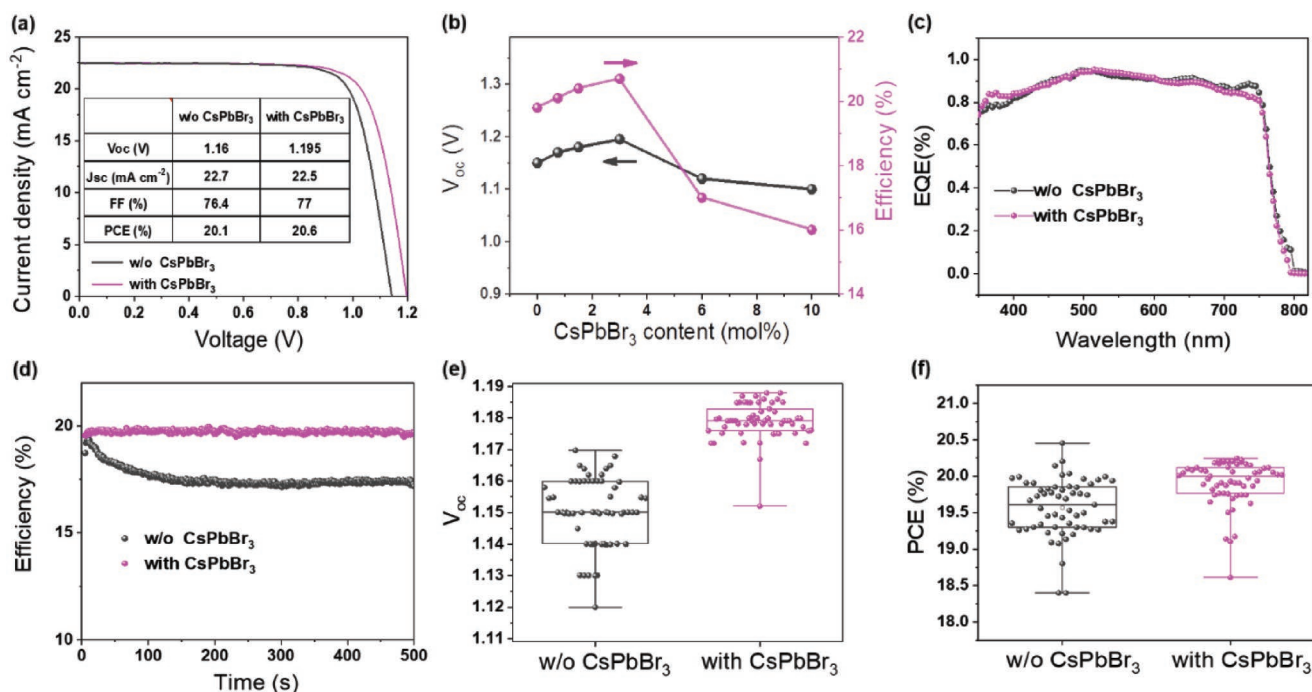
**ADVANCED
SCIENCE NEWS**

www.advancedsciencenews.com

**ADVANCED
FUNCTIONAL
MATERIALS**

www.afm-journal.de

**Figure 4.** Photovoltaic performance of PSCs. a) J–V curves of the devices w/o CsPbBr$_3$ and with CsPbBr$_3$ (3% mol). Performance parameters are listed in the inset. b) Open-circuit voltage ($V_{oc}$) (dark grey) and J–V efficiency (pink) of the devices as a function of content of CsPbBr$_3$ colloidal additives. c) EQE spectra of the devices w/o CsPbBr$_3$ (dark grey) and with CsPbBr$_3$ (3% mol) (pink). d) The steady-state output of the devices w/o CsPbBr$_3$ (dark grey) and with CsPbBr$_3$ (3% mol) (pink). e) Statistics of the $V_{oc}$ and f) PCE of devices w/o CsPbBr$_3$ (dark grey) and with CsPbBr$_3$ (3%) (pink).

quantum efficiency (EQE) results (22.2 and 21.9 mA cm$^{-2}$ for device w/o and with CsPbBr$_3$, respectively; Figure 4c). For the steady-state output measurement, device w/o CsPbBr$_3$ shows a rapid burn-in decay from 19.3% to 17.5% in the initial 200 s, while device with CsPbBr$_3$ maintains a stabilized efficiency of 19.8% for exceeding 500 s without any burn-in decay (Figure 4d). Burn-in loss has been widely reported in organic solar cells and the mechanism may be photo-induced sub-bandgap states with increased energy disorder in active layer.[52] For PSCs, the initial exponential decay can be reduced by bulk defects passivation,[29] GB passivation,[53] and electron transport layer (ETL)/hole transport layer (HTL) modification.[54] The hysteresis of the devices are measured as well and the results are shown in Figure S7 and Table S1 (Supporting Information). Furthermore, the statistical distributions of performance parameters for 60 devices without and with CsPbBr$_3$ are shown in Figure 4e, f and Figure S8 (Supporting Information). The average $V_{oc}$ and PCE are enhanced for devices with CsPbBr$_3$ as compared to the control devices.

The investigation of long-term operational stability is crucial for application of PSCs. Then, we move on to study the devices under MPP steady-state output operation (by setting the voltage to MPP voltage and then track the current density in real time) and under continuous light illumination (AM 1.5G) in nitrogen-filled glovebox. In **Figure 5**a, the device w/o CsPbBr$_3$ shows around 20% efficiency loss after 140 h operation (an exponential decay followed by a linear decay with a 0.14% h$^{-1}$ slope), while the device with CsPbBr$_3$ demonstrates a superior operational stability by maintaining 90% of its initial efficiency exceeding 500 h continuous output (a linear decay with a 0.016% h$^{-1}$ scope). This result highlights

the benefit of CsPbBr$_3$ on the remarkably enhanced stability. Additionally, temperature is proven to have a critical influence on the stability of PSCs and degradation is often accelerated under heat.[24] Therefore, thermal and operational stability were measured simultaneously on a hotplate of 65 °C in glovebox still under MPP continuous operation and light illumination. The device with CsPbBr$_3$ demonstrates a much longer stability by remaining 80% performance after 125 h operation, compared to the device w/o CsPbBr$_3$ (70% of its initial value after 80 h). For comparison, in **Table 1**, the published operational stability results of CsFAMA PSCs are listed,[21,28,35,55–58] and here, we report the longest thermal operational stability in planar type TiO$_2$-based PSCs with Spiro-OMeTAD. Additionally, the device stability under humid condition (40%–50% humidity) was also enhanced (Figure S9, Supporting Information).

## 2.5. Further Analysis on the Fundamental Reason to the Improvement of CsPbBr$_3$-Passivated CsFAMA Perovskite Solar Cell Devices

To gain an insight into the remarkably enhanced open-circuit voltage and operational stability for CsPbBr$_3$-cluster passivated PSC devices, electrochemical impedance spectroscopy measurements are performed.[59,60] The experiment data can be fitted (Figure S10, Supporting Information) by using an equivalent circuit (inset of **Figure 6**a) and then the related recombination time constant ($\tau_{rec} = R_{rec} \times C_{rec}$) can be extracted (Figure 6a, b). Two time constants, which were assigned to the
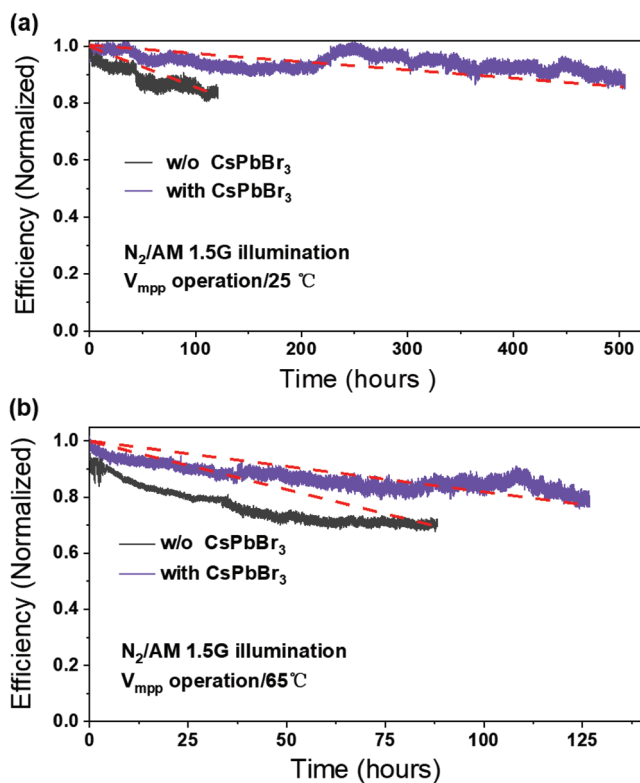
**ADVANCED
SCIENCE NEWS**
www.advancedsciencenews.com

**ADVANCED
FUNCTIONAL
MATERIALS**
www.afm-journal.de

**Figure 5.** Operational stability of PSCs. a) Steady-state output of PSCs under continuous MPP operation and AM 1.5G illumination for 500 h in nitrogen-filled glovebox. b) Steady-state output of PSCs under continuous MPP operation, AM 1.5G illumination, and thermal stress for 125 h in nitrogen-filled glovebox. The devices are putting on a hot plate and the temperature of devices' surface are monitored as 65 °C. The fluctuation in curves is mainly due to the variation of the light intensity of the solar simulator.

surface charge recombination ($\tau_{sur}$) and bulk charge recombination ($\tau_{bulk}$), were extracted under different bias voltage (from 1 to −0.6 V). $\tau_{bulk}$ shows little variation between the two devices w/o CsPbBr$_3$ and with CsPbBr$_3$, while $\tau_{surface}$ (ranging from 0 to −0.6 V) increases about two times after CsPbBr$_3$ passivation. As is known, the built-in electric field in devices will be enhanced under negative bias voltage and ionic transport can be accelerated in perovskite, inducing excess accumulated trap states and unexpected non-radiative recombination centers. According to this, the enhanced $\tau_{surface}$ under negative bias voltage strongly indicates reduced trap states at surface/interface in passivated perovskite film. In Figure 6c,d, the devices with CsPbBr$_3$ show lower densities of trap states [denoted as $N = \int Nt dE(E = E_t − E_c)$, Note S2, Supporting Information] before and after long-term stability operation, especially after 500 h continuous operation. Quantitatively, the devices w/o CsPbBr$_3$ shows an increased defect state densities about $1 \times 10^{20}$ cm$^{-3}$ after 150 h continuous operation, while the number is only about $4 \times 10^{19}$ cm$^{-3}$ after 500 h in device with CsPbBr$_3$.

Ion migration has been demonstrated to be the major factor causing the degradation of PSCs under operation condition.[49] We speculate that the improvement in operational stability and reduced trap states is mainly originated from the inhibited ion

migration by introducing CsPbBr$_3$ clusters. Then cryogenic Galvanostatic with voltage–current measurements under a wide temperature range (100–295 K) (**Figure 7**a) are conducted to obtain the ion migration barrier of perovskite films w/o CsPbBr$_3$ and with CsPbBr$_3$. The energy barrier of ion migration ($E_a$) can be derived from equation (1)[26,44,61]:

$$\sigma_{ion}(T)T = ne\mu = \frac{Z_i e^2 N_A C_{v0} D_0}{k_B V_m} \exp\left(-\frac{G_v}{5k_B T}\right) \exp\left(-\frac{E_a}{k_B T}\right) = \sigma_0 \exp\left(\frac{E_a^{eff}}{k_B T}\right) \tag{1}$$

by extracting the slope of $\ln(\sigma_{ion}T)\sim 1/T$ curve. The $E_a$ for sample with CsPbBr$_3$ is about 0.23 eV, larger than 0.17 eV for sample w/o CsPbBr$_3$. Since GBs and surface are the dominant channel for ion migration,[41] therefore, larger $E_a$ means effectively suppressed migration of ions and reduced defect states. Additionally, compared to the phase segregation in the sample w/o CsPbBr$_3$ (Figure 1), the phase segregation was notably weakened in the sample with CsPbBr$_3$. In the passivated films, after 80 s electric poling duration, the PL peak position shows only several nm shift (Figure 7b–d) and (Figure S11a, Supporting Information). Compared to the control sample without CsPbBr$_3$ passivation, where PL peak shifts almost 30 nm after poling (Figure S1b, Supporting Information), the phase segregation behavior is significantly suppressed in our newly developed devices. The entire film also exhibits uniform iodide/bromide/cesium distribution after poling (Figure S11b, Supporting Information), which also strongly suggests the suppressed ion migration and phase segregation with CsPbBr$_3$ passivation. The suppressed phase segregation is associated with the inhibited ion migration by inorganic part protection with larger ion migration barrier. These findings strongly suggest that the inhibited ion migration contributes to the improved operational stability of CsPbBr$_3$ passivated PSCs.

To sufficiently demonstrate the CsPbBr$_3$-cluster plays a key role for inhibited ion migration and enhanced stability, we further performed HADDF and EDS characterization of the passivated film after 500 h stability test. In Figure S12 in the Supporting Information, we can still find a cluster-distribution mapping in HADDF and EDS images, which strongly suggests that the perovskite film remains its initial structure after long-term operation under illumination. This is consistent with the higher activation energy barrier and eliminated phase segregation for passivated samples. Further, to validate the importance of CsPbBr$_3$-cluster via our adding CsPbBr$_3$ colloidal solution method, PCSs with the same amount of CsPbBr$_3$ powder additive are fabricated as a control experiment (Figure S13, Supporting Information). As mentioned in Figures S3 and S4 in the Supporting Information, powder additive will cause an total incorporation of added Cs$^+$ and Br$^-$ into bulk CsFAMA crystals. As a result, the solar cells made from powder additive shows a lower $V_{oc}$ around 30 meV. Further, for the operational stability, solar cells with powder additive lags far behind the device compared with the devices with CsPbBr$_3$ solution additive. Collectively, these results strongly indicate the forming of CsPbBr$_3$-cluster by CsPbBr$_3$ colloidal solution method plays an important role for the improved efficiency and stability in passivated PSCs.

**Table 1.** Operational stability of the CsPbBr$_3$-cluster passivated PSCs as compared to previous works of CsFAMA PSCs.

| Perovksite composition | Device type | Working state | Ambient condition | Temperature (°C) | Stability (h) | Published works |
|---|---|---|---|---|---|---|
| Cs$_{0.05}$FA$_{0.80}$MA$_{0.15}$ Pb(I$_{0.85}$Br$_{0.15}$)$_3$ | FTO/m-TiO$_2$/c-TiO$_2$/ PVK/Spiro/Au | Continuous light/ MMPT | N$_2$ | RT | T$_{90}$ > 250 | Lee et al.[18] |
| Cs$_{0.05}$FA$_{0.80}$MA$_{0.15}$ Pb(I$_{0.85}$Br$_{0.15}$)$_3$+Rb5% | FTO/m-TiO$_2$/c-TiO$_2$/ PVK/Spiro/Au | Continuous light/ MMPT | N$_2$ | 85 | T$_{95}$ = 500 | Peters et al.[52] |
| Cs$_{0.05}$FA$_{0.80}$MA$_{0.15}$ Pb(I$_{0.85}$Br$_{0.15}$)$_3$ | FTO/m-TiO$_2$/c-TiO$_2$/ PVK/Spiro/Au | Continuous light/ MMPT | N$_2$ | 25 | T$_{80}$ = 60 | Xu et al.[53] |
| Cs$_{0.05}$FA$_{0.80}$MA$_{0.15}$ Pb(I$_{0.85}$Br$_{0.15}$)$_3$ | ITO/c-TiO$_2$/PVK/ Spiro/Au | Continuous light/ MMPT/UV filter | N$_2$ | RT | T$_{90}$ = 500 | Ip et al.[54] |
| Cs$_{0.05}$FA$_{0.80}$MA$_{0.15}$ Pb(I$_{0.85}$Br$_{0.15}$)$_3$ | FTO/m-TiO$_2$/c-TiO$_2$/ PVK/CuSCN/rGo/Au | Continuous light/ MMPT | N$_2$ | 60 | T$_{100}$ = 500 | Lee et al.[32] |
| Cs$_{0.05}$FA$_{0.80}$MA$_{0.15}$ Pb(I$_{0.85}$Br$_{0.15}$)$_3$ | FTO/m-TiO$_2$/c-TiO$_2$/ PVK/Spiro/Au | Continuous light/MMPT | N$_2$ | 60 | T$_{90}$ = 400 | Lee et al.[32] |
| Cs$_{0.06}$FA$_{0.79}$MA$_{0.15}$ Pb(I$_{0.85}$Br$_{0.15}$)$_3$+K10% | FTO/m-TiO$_2$/c-TiO$_2$/ PVK/Spiro/Au | Continuous light/ MMPT/UV filter | N$_2$ | 40 | T$_{80}$ = 400 | Christians et al.[25] |
| Cs$_{0.05}$FA$_{0.80}$MA$_{0.15}$ Pb(I$_{0.85}$Br$_{0.15}$)$_3$ | FTO/m-TiO$_2$/c-TiO$_2$/ PVK/Spiro/Au | Continuous light/ MMPT | N$_2$ | RT | T$_{90}$ > 500 | Saliba et al.[55] |
| Cs$_{0.05}$FA$_{0.80}$MA$_{0.15}$ Pb(I$_{0.85}$Br$_{0.15}$)$_3$ | ITO/c-TiO$_2$/PVK/ Spiro/Au | Continuous light/ MMPT/UV filter | N$_2$ | 25 | T$_{90}$ = 500 | This work |
| Cs$_{0.05}$FA$_{0.80}$MA$_{0.15}$ Pb(I$_{0.85}$Br$_{0.15}$)$_3$ | ITO/c-TiO$_2$/PVK/ Spiro/Au | Continuous light/ MMPT/UV filter | N$_2$ | 65 | T$_{80}$ = 125 | This work |
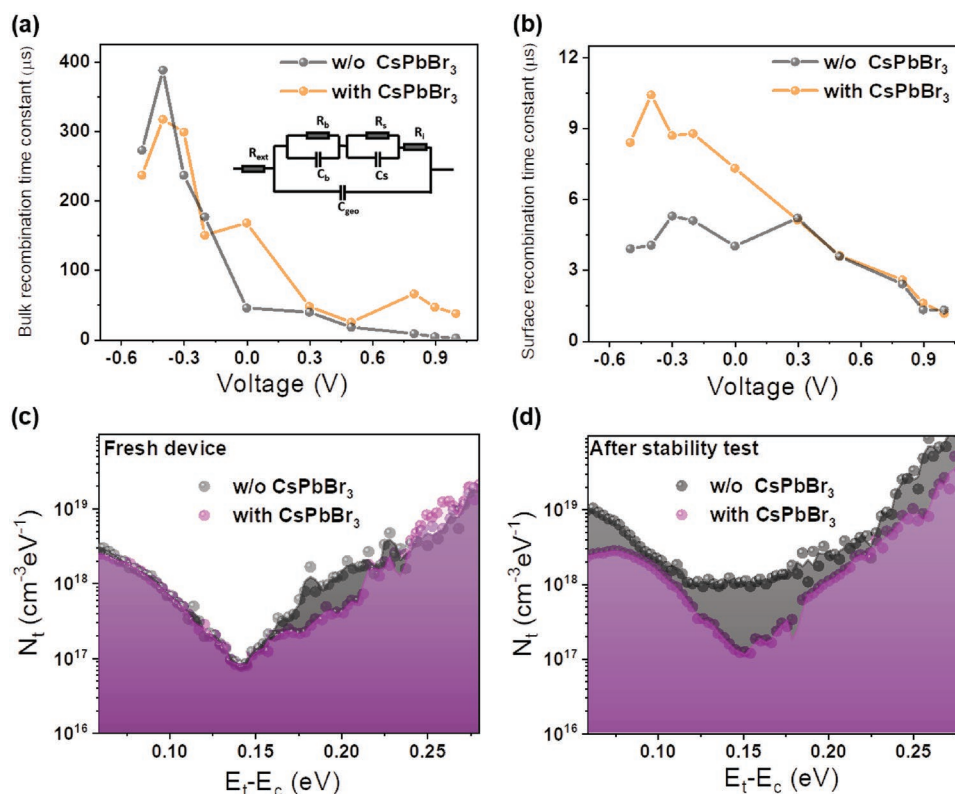


**Figure 6.** Impendence spectroscopy characterization of PSCs. a) Bulk recombination time constant and b) surface recombination time constant of fresh devices w/o CsPbBr$_3$ (grey) and with CsPbBr$_3$ (3% mol) (orange) under different applied bias. Inset of a): the equivalent circuits for impedance spectra fitting. c,d) Trap density of states of the devices w/o CsPbBr$_3$ (dark grey) and with CsPbBr$_3$ (violet) before c) and after d) corresponding operational long-term stability test.

**ADVANCED
SCIENCE NEWS**
www.advancedsciencenews.com

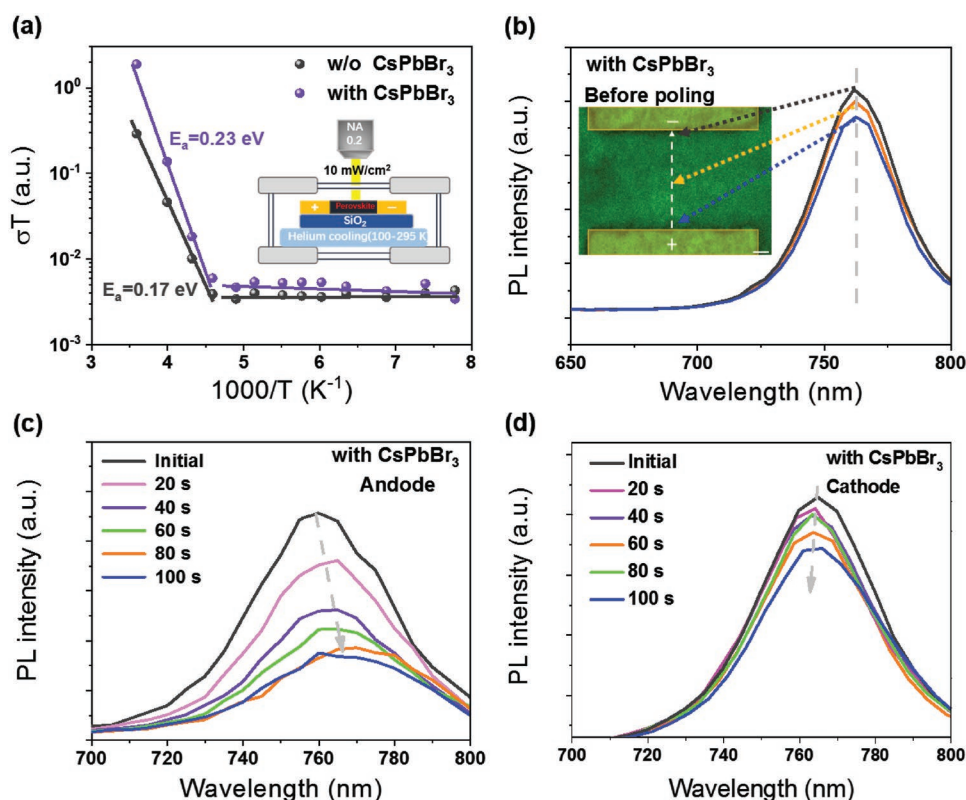**ADVANCED
FUNCTIONAL
MATERIALS**
www.afm-journal.de

**Figure 7.** Ion migration characterization of $CsPbBr_3$-cluster passivated perovskite films. a) Temperature-dependent conductivity of samples w/o $CsPbBr_3$ (dark grey) and with $CsPbBr_3$ (3% mol) (violet) under light illumination. Inset: scheme of experimental set-up. b) PL spectra of the sample with $CsPbBr_3$ before electric poling. The inset shows PL emission image and the three selected positions. c) PL spectra at the positive pole (anode) after various poling durations. d) PL spectra at the negative pole (cathode) after various poling durations.

## 3. Conclusion

In summary, we systematically investigated the phase segregation phenomenon in the state-of-art CsFAMA polycrystalline film. Then, we demonstrated a solution method to constitute a $CsPbBr_3$-cluster passivated perovskite structure of high-quality CsFAMA films. The $CsPbBr_3$ clusters lead to longer carrier lifetime, larger activation energy for ionic motion, and inhibited phase segregation. As a result, the fabricated high-performance planar passivated PSCs showed best PCE with 20.6% and the champion $V_{OC}$ of 1.195 V, corresponding to a quite low loss-in potential of 0.42 V. The operational stability under 25 °C was enhanced significantly, with the $T_{90}$ lifetime boosted to 500 h, rather than 70 h for control samples. More remarkably, we report the first thermal plus operational stability $T_{80}$ = 125 h in planar-type $TiO_2$-based CsFAMA PSCs under 65 °C, MPP tracking and continuous light illumination. Our approach to utilize $CsPbBr_3$ clusters around perovskite grains will inspire further new routes to design PSCs with core–shell structure to achieve high stability and longevity. This work also highlights the significance of inorganic perovskite in suppressing ionic motion in triple cation PSCs.

## 4. Experimental Section

*Planar Perovskite Solar Cell Fabrication and Characterization*: Indium doped tin oxide (ITO)-coated glasses were cleaned by ultrasonic cleaner using acetone and isopropanol (IPA). Then, $TiO_2$-Cl colloid solution was spin-coated on the substrates at 3000 rpm for 30 s twice. Finally, the substrates were annealed at 150 °C for 30 min in ambient air. After annealing, the $TiO_2$-coated substrates were transferred into $N_2$-filled glove box. For the CsFAMA control perovskite layer with different amount of $CsPbBr_3$ additive, first, the $Cs_{0.05}FA_{0.80}MA_{0.15}PbI_{2.55}Br_{0.45}$ precursor solution (1.4 m, DMF:DMSO = 4:1,volume) was prepared with molar ratios of both $PbI_2/PbBr_2$ and FAI/MABr fixed at 0.85:0.15, molar ratio of CsI/(FAI + MABr) at 0.05:0.95, and the molar ratio of (FAI + MABr + CsI)/ ($PbI_2$ + $PbBr_2$) at 1:1. The CsFAMA precursor solution was stirring for 30 min at 60 °C. For the CsFAMA perovskite film with 3% $CsPbBr_3$ solution additive, the $CsPbBr_3$ precursor solution (0.43 m) was prepared with molar ratio of $PbBr_2$/CsBr fixed at 1:1 and stirred lasting for 1 h at 80 °C. Then, different amount of $CsPbBr_3$ precursor solution were added into the as-prepared CsFAMA precursor solution. For the CsFAMA perovskite film with 3% $CsPbBr_3$ powder additive, the preparation is the same with CsFAMA control sample just with different CsI/CsBr/FAI/MABr/$PbI_2$/ $PbBr_2$ ratio to form the target perovskite precursor solution (1.4 m, DMF:DMSO = 4:1,volume). All the perovskite films were fabricated on the $TiO_2$ substrates with a spin-coating procedure. First, the process was carried out at 2300 rpm for 15 s with an acceleration of 220 rpm $s^{-1}$. Then, it was carried out at 5500 rpm for 50 s with a ramp-up of 2000 rpm $s^{-1}$. Chlorobenzene (110 μL) was dropped on the substrate during the second step at 20 s before the end. Then, the substrates were immediately heated at 100 °C for 40 min. The Spiro-OMeTAD solution was dropped on the top of perovskite film to form hole-transport layer with a spinning at 3000 rpm for 30 s. At last, around 80 nm Au electrode was thermally evaporated to form top electrode.

The *J–V* curves were measured by a solar simulator (Solar IV-150A, Zolix) and an Agilent B2912 source/measure unit. Light intensity was calibrated with a Newport calibrated KG5-filtered Si reference cell.

The active area of the PSCs is 0.049 cm². The *J–V* curves were tested from 1.2 to −0.01 V (reverse) or from −0.01 to 1.2 V (forward) with a scan velocity of 50 mV s$^{-1}$ (voltage step of 10 mV and delay time of 200 ms). For the steady-state output test, efficiency was test by setting the voltage to the MPP voltage and then track the current density in glovebox. The operational stability test at continuous operation and AM 1.5G illumination was carried out in glovebox at a constant device temperature of 25 °C by setting voltage to MPP and tracking the current output. A 420 nm cut-off UV filter was applied. For the thermal plus operational stability test, the devices were putting on a hot plate of 65 °C also at continuous MPP conditions and AM 1.5G illumination in a nitrogen-filled glovebox.

For the EQE measurement, first, the standard silicon solar cell was used to scan under 300–850 nm laser in Zolix Solar Cell Scan 100 IPCE Measurement System. The device was put into a self-made box flowed with nitrogen and then the box was put into a Zolix Solar Cell Scan 100 IPCE Measurement System. The scan range was 300–850 nm, and recorded data every 5 nm. The impedance spectrum was measured using a potentiostat/galvanostat (SP-150, Bio-Logic, France). The frequency can be tuned from 10 Hz to 1 MHz with 200 data points.

*Film Characterization*: For the in situ phase segregation characterization and temperature-dependent conductivity measurement of perovskite film, lateral Au/perovskite/Au device was prepared, the thickness of the gold electrodes was approximately 0.1 µm, and the gap between the two gold electrodes was 30 µm. Then, perovskite film was spin-coated on the substrates followed by annealing process. Then 100 nm PMMA was spin-coated on all of the perovskite films to isolate water and oxygen. For in situ phase segregation study, an Olympus FV3000 CLSM was used. A 488 nm laser diode was chosen as light source and a 40 × dry objective (LUCPLFLN40X, 0.6 NA, WD 2.7-4.0) was employed. Meanwhile, Agilent B2912 source unit was used to conduct galvanostatic measurement. The PL emission was collected by the same objective and detected by photomultiplier. For details of temperature-dependent conductivity measurement in the lateral structure, please refer to Conings et al.[23]

PL spectra and time resolved photoluminescence (TRPL) decay spectra were measured using an Edinburgh Instruments Ltd. FLS980 fluorescence spectrometer system. The perovskite films were prepared on glass. The surface and cross-sectional morphology of the perovskite films and device were recorded by an SEM (Quanta FEG 450) under 10 kV electron beam accelerate voltage. A PANalytical X'Pert3 Powder X-ray diffractometer system using monochromatized Cu K$\alpha$ radiation ($\lambda$ = 1.5406 Å) was used to collect XRD patterns of perovskite films. HAADF images and EDS mappings were acquired at an aberration-corrected FEI (Titan Cubed Themis G2) operated at 300 kV equipped with an X-FEG gun and Bruker Super-X EDX detectors.

## Supporting Information

Supporting Information is available from the Wiley Online Library or from the author.

## Acknowledgements

## Conflict of Interest

The authors declare no conflict of interest.

[1] A. Kojima, K. Teshima, Y. Shirai, T. Miyasaka, *J. Am. Chem. Soc.* **2009**, *131*, 6050.

[2] H.-S. Kim, C.-R. Lee, J.-H. Im, K.-B. Lee, T. Moehl, A. Marchioro, S.-J. Moon, R. Humphry-Baker, J.-H. Yum, J. E. Moser, M. Grätzel, N.-G. Park, *Sci. Rep.* **2012**, *2*, 591.

[3] J. Burschka, N. Pellet, S.-J. Moon, R. Humphry-Baker, P. Gao, M. K. Nazeeruddin, M. Grätzel, *Nature* **2013**, *499*, 316.

[4] F. Hao, C. C. Stoumpos, Z. Liu, R. P. H. Chang, M. G. Kanatzidis, *J. Am. Chem. Soc.* **2014**, *136*, 16411.

[5] J.-H. Im, I.-H. Jang, N. Pellet, M. Grätzel, N.-G. Park, *Nat. Nanotechnol.* **2014**, *9*, 927.

[6] S. D. Stranks, H. J. Snaith, *Nat. Nanotechnol.* **2015**, *10*, 391.

[7] Y. C. Kim, K. H. Kim, D.-Y. Son, D.-N. Jeong, J.-Y. Seo, Y. S. Choi, I. T. Han, S. Y. Lee, N.-G. Park, *Nature* **2017**, *550*, 87.

[8] C. Zuo, H. J. Bolink, H. Hong, J. Huang, D. Cahen, L. Ding, *Adv. Sci.* **2016**, *3*, 1500324.

[9] Q. Dong, Y. Fang, Y. Shao, P. Mulligan, J. Qiu, L. Cao, J. Huang, *Science* **2015**, *347*, 967.

[10] M. Hu, C. Bi, Y. Yuan, Z. Xiao, Q. Dong, Y. Shao, J. Huang, *Small* **2015**, *11*, 2164.

[11] A. Miyata, A. Mitioglu, P. Plochocka, O. Portugall, J. T.-W. Wang, S. D. Stranks, H. J. Snaith, R. J. Nicholas, *Nat. Phys.* **2015**, *11*, 582.

[12] L. M. Pazos-Outón, M. Szumilo, R. Lamboll, J. M. Richter, M. Crespo-Quesada, M. Abdi-Jalebi, H. J. Beeson, M. Vrućinić, M. Alsari, H. J. Snaith, B. Ehrler, R. H. Friend, F. Deschler, *Science* **2016**, *351*, 1430.

[13] W.-J. Yin, T. Shi, Y. Yan, *Adv. Mater.* **2014**, *26*, 4653.

[14] Z. Fang, S. Wang, S. Yang, L. Ding, *Inorg. Chem. Front.* **2018**, *5*, 1690.

[15] X. Jia, L. Ding, *Sci. China Mater.* **2019**, *62*, 54.

[16] G. E. Eperon, S. D. Stranks, C. Menelaou, M. B. Johnston, L. M. Herz, H. J. Snaith, *Energy Environ. Sci.* **2014**, *7*, 982.

[17] C. C. Stoumpos, C. D. Malliakas, M. G. Kanatzidis, *Inorg. Chem.* **2013**, *52*, 9019.

[18] J.-W. Lee, D.-H. Kim, H.-S. Kim, S.-W. Seo, S. M. Cho, N.-G. Park, *Adv. Energy Mater.* **2015**, *5*, 1501310.

[19] D. P. McMeekin, G. Sadoughi, W. Rehman, G. E. Eperon, M. Saliba, M. T. Hörantner, A. Haghighirad, N. Sakai, L. Korte, B. Rech, M. B. Johnston, L. M. Herz, H. J. Snaith, *Science* **2016**, *351*, 151.

[20] N. J. Jeon, J. H. Noh, W. S. Yang, Y. C. Kim, S. Ryu, J. Seo, S. I. Seok, *Nature* **2015**, *517*, 476.

[21] M. Saliba, T. Matsui, J.-Y. Seo, K. Domanski, J.-P. Correa-Baena, M. K. Nazeeruddin, S. M. Zakeeruddin, W. Tress, A. Abate, A. Hagfeldt, M. Grätzel, *Energy Environ. Sci.* **2016**, *9*, 1989.

[22] A. Amat, E. Mosconi, E. Ronca, C. Quarti, P. Umari, M. K. Nazeeruddin, M. Grätzel, F. De Angelis, *Nano Lett.* **2014**, *14*, 3608.

[23] B. Conings, J. Drijkoningen, N. Gauquelin, A. Babayigit, J. D'Haen, L. D'Olieslaeger, A. Ethirajan, J. Verbeeck, J. Manca, E. Mosconi, F. D. Angelis, H.-G. Boyen, *Adv. Energy Mater.* **2015**, *5*, 1500477.

[24] G. Divitini, S. Cacovich, F. Matteocci, L. Cinà, A. Di Carlo, C. Ducati, *Nat. Energy* **2016**, *1*, 15012.

[25] J. A. Christians, P. A. Miranda Herrera, P. V. Kamat, *J. Am. Chem. Soc.* **2015**, *137*, 1530.

**ADVANCED
SCIENCE NEWS**

www.advancedsciencenews.com

**ADVANCED
FUNCTIONAL
MATERIALS**

www.afm-journal.de

[26] Y.-C. Zhao, W.-K. Zhou, X. Zhou, K.-H. Liu, D.-P. Yu, Q. Zhao, *Light: Sci. Appl.* **2017**, *6*, e16243.

[27] K. Domanski, E. A. Alharbi, A. Hagfeldt, M. Grätzel, W. Tress, *Nat. Energy* **2018**, *3*, 61.

[28] M. Abdi-Jalebi, Z. Andaji-Garmaroudi, S. Cacovich, C. Stavrakas, B. Philippe, J. M. Richter, M. Alsari, E. P. Booker, E. M. Hutter, A. J. Pearson, S. Lilliu, T. J. Savenije, H. Rensmo, G. Divitini, C. Ducati, R. H. Friend, S. D. Stranks, *Nature* **2018**, *555*, 497.

[29] M. I. Saidaminov, J. Kim, A. Jain, R. Quintero-Bermudez, H. Tan, G. Long, F. Tan, A. Johnston, Y. Zhao, O. Voznyy, E. H. Sargent, *Nat. Energy* **2018**, *3*, 648.

[30] Y. Zhao, J. Wei, H. Li, Y. Yan, W. Zhou, D. Yu, Q. Zhao, *Nat. Commun.* **2016**, *7*, 10228.

[31] J. A. Christians, P. Schulz, J. S. Tinkham, T. H. Schloemer, S. P. Harvey, B. J. Tremolet de Villers, A. Sellinger, J. J. Berry, J. M. Luther, *Nat. Energy* **2018**, *3*, 68.

[32] J.-W. Lee, Z. Dai, T.-H. Han, C. Choi, S.-Y. Chang, S.-J. Lee, N. De Marco, H. Zhao, P. Sun, Y. Huang, Y. Yang, *Nat. Commun.* **2018**, *9*, 3021.

[33] W. Li, C. Zhang, Y. Ma, C. Liu, J. Fan, Y. Mai, R. E. I. Schropp, *Energy Environ. Sci.* **2018**, *11*, 286.

[34] X. Zheng, B. Chen, J. Dai, Y. Fang, Y. Bai, Y. Lin, H. Wei, X. C. Zeng, J. Huang, *Nat. Energy* **2017**, *2*, 17102.

[35] N. Arora, M. I. Dar, A. Hinderhofer, N. Pellet, F. Schreiber, S. M. Zakeeruddin, M. Grätzel, *Science* **2017**, *358*, 768.

[36] K. Domanski, B. Roose, T. Matsui, M. Saliba, S.-H. Turren-Cruz, J.-P. Correa-Baena, C. R. Carmona, G. Richardson, J. M. Foster, F. De Angelis, J. M. Ball, A. Petrozza, N. Mine, M. K. Nazeeruddin, W. Tress, M. Grätzel, U. Steiner, A. Hagfeldt, A. Abate, *Energy Environ. Sci.* **2017**, *10*, 604.

[37] G. Y. Kim, A. Senocrate, T.-Y. Yang, G. Gregori, M. Grätzel, J. Maier, *Nat. Mater.* **2018**, *17*, 445.

[38] E. T. Hoke, D. J. Slotcavage, E. R. Dohner, A. R. Bowring, H. I. Karunadasa, M. D. McGehee, *Chem. Sci.* **2015**, *6*, 613.

[39] Z. Xiao, Y. Yuan, Y. Shao, Q. Wang, Q. Dong, C. Bi, P. Sharma, A. Gruverman, J. Huang, *Nat. Mater.* **2015**, *14*, 193.

[40] Y. Zhao, W. Zhou, H. Tan, R. Fu, Q. Li, F. Lin, D. Yu, G. Walters, E. H. Sargent, Q. Zhao, *J. Phys. Chem. C* **2017**, *121*, 14517.

[41] Y. Shao, Y. Fang, T. Li, Q. Wang, Q. Dong, Y. Deng, Y. Yuan, H. Wei, M. Wang, A. Gruverman, J. Shield, J. Huang, *Energy Environ. Sci.* **2016**, *9*, 1752.

[42] Z. Chu, M. Yang, P. Schulz, D. Wu, X. Ma, E. Seifert, L. Sun, X. Li, K. Zhu, K. Lai, *Nat. Commun.* **2017**, *8*, 2230.

[43] P. Wang, X. Zhang, Y. Zhou, Q. Jiang, Q. Ye, Z. Chu, X. Li, X. Yang, Z. Yin, J. You, *Nat. Commun.* **2018**, *9*, 2225.

[44] Q. Zeng, X. Zhang, X. Feng, S. Lu, Z. Chen, X. Yong, S. A. T. Redfern, H. Wei, H. Wang, H. Shen, W. Zhang, W. Zheng, H. Zhang, J. S. Tse, B. Yang, *Adv. Mater.* **2018**, *30*, 1705393.

[45] W. Zhou, Y. Zhao, X. Zhou, R. Fu, Q. Li, Y. Zhao, K. Liu, D. Yu, Q. Zhao, *J. Phys. Chem. Lett.* **2017**, *8*, 4122.

[46] Q. Zeng, X. Zhang, C. Liu, T. Feng, Z. Chen, W. Zhang, W. Zheng, H. Zhang, B. Yang, *Sol. RRL* **2018**, DOI:10.1002/solr.201800239.

[47] X. Tang, M. van den Berg, E. Gu, A. Horneber, G. J. Matt, A. Osvet, A. J. Meixner, D. Zhang, C. J. Brabec, *Nano Lett.* **2018**, *18*, 2172.

[48] T.-Y. Yang, G. Gregori, N. Pellet, M. Grätzel, J. Maier, *Angew. Chem.* **2015**, *127*, 8016.

[49] Y. Yuan, J. Huang, *Acc. Chem. Res.* **2016**, *49*, 286.

[50] J. Liang, C. Wang, Y. Wang, Z. Xu, Z. Lu, Y. Ma, H. Zhu, Y. Hu, C. Xiao, X. Yi, G. Zhu, H. Lv, L. Ma, T. Chen, Z. Tie, Z. Jin, J. Liu, *J. Am. Chem. Soc.* **2016**, *138*, 15829.

[51] K. Yan, M. Long, T. Zhang, Z. Wei, H. Chen, S. Yang, J. Xu, *J. Am. Chem. Soc.* **2015**, *137*, 4460.

[52] C. H. Peters, I. T. Sachs-Quintana, W. R. Mateker, T. Heumueller, J. Rivnay, R. Noriega, Z. M. Beiley, E. T. Hoke, A. Salleo, M. D. McGehee, *Adv. Mater.* **2012**, *24*, 663.

[53] J. Xu, A. Buin, A. H. Ip, W. Li, O. Voznyy, R. Comin, M. Yuan, S. Jeon, Z. Ning, J. J. McDowell, P. Kanjanaboos, J.-P. Sun, X. Lan, L. N. Quan, D. H. Kim, I. G. Hill, P. Maksymovych, E. H. Sargent, *Nat. Commun.* **2015**, *6*, 7081.

[54] A. H. Ip, L. N. Quan, M. M. Adachi, J. J. McDowell, J. Xu, D. H. Kim, E. H. Sargent, *Appl. Phys. Lett.* **2015**, *106*, 143902.

[55] M. Saliba, T. Matsui, K. Domanski, J.-Y. Seo, A. Ummadisingu, S. M. Zakeeruddin, J.-P. Correa-Baena, W. R. Tress, A. Abate, A. Hagfeldt, M. Grätzel, *Science* **2016**, *354*, 206.

[56] E. H. Anaraki, A. Kermanpur, L. Steier, K. Domanski, T. Matsui, W. Tress, M. Saliba, A. Abate, M. Grätzel, A. Hagfeldt, J.-P. Correa-Baena, *Energy Environ. Sci.* **2016**, *9*, 3128.

[57] H. Tan, A. Jain, O. Voznyy, X. Lan, F. P. García de Arquer, J. Z. Fan, R. Quintero-Bermudez, M. Yuan, B. Zhang, Y. Zhao, F. Fan, P. Li, L. N. Quan, Y. Zhao, Z.-H. Lu, Z. Yang, S. Hoogland, E. H. Sargent, *Science* **2017**, *355*, 722.

[58] M. M. Tavakoli, W. Tress, J. V. Milić, D. Kubicki, L. Emsley, M. Grätzel, *Energy Environ. Sci.* **2018**, *11*, 3310.

[59] H.-S. Kim, I. Mora-Sero, V. Gonzalez-Pedro, F. Fabregat-Santiago, E. J. Juarez-Perez, N.-G. Park, J. Bisquert, *Nat. Commun.* **2013**, *4*, 2242.

[60] A. Dualeh, T. Moehl, N. Tétreault, J. Teuscher, P. Gao, M. K. Nazeeruddin, M. Grätzel, *ACS Nano* **2014**, *8*, 362.

[61] J. Mizusaki, K. Arai, K. Fueki, *Solid State Ionics* **1983**, *11*, 203.